

# Supplementary material for "Thermal softening induced subduction initiation at a passive margin"

Dániel Kiss<sup>1</sup>, Lorenzo G. Candiotti<sup>1</sup>, Thibault Duretz<sup>2,1</sup> and Stefan M. Schmalholz<sup>1</sup>

<sup>1</sup> *Institute of Earth Sciences, University of Lausanne, 1015 Lausanne, Switzerland*

<sup>2</sup> *Univ. Rennes, CNRS, Géosciences Rennes - UMR 6118, F-35000 Rennes, France*

15 December 2019

## Contents of this file

- (i) Governing equations
- (ii) Table S1
- (iii) Figures S1, S2, S3, S4 and S5
- (iv) Movie S1

## Introduction

This supporting material provides the description of the equations used in the numerical model, five additional figures and a table with the applied model parameters. Table S1 describes the parameters used for the simulations presented in the main article and also the parameters which have been used for simulations shown in Figures S1 to S4. Figure S1, S2, S3 and S4 show the structural, thermal and stress evolution of models (1), (2), (3) and (4), respectively. Figure S5 shows the evolution of the horizontal driving force for each simulations. Movie S1 shows the evolution of temperature and dissipation in model (1).

## 1 GOVERNING EQUATIONS (Schmalholz et al., 2019)

The governing system of partial differential equations is solved numerically with a finite-difference / marker-in-cell method (e.g. Gerya & Yuen, 2003). The diffusive terms in the force balance and heat transfer equations are discretised on an Eulerian staggered grid while advection and rotation terms are treated explicitly using a set of Lagrangian markers and a 4th order in space / 1st order in time Runge-Kutta scheme.

The model topography is a material interface defined by a Lagrangian marker chain which is displaced with the numerically calculated velocity field (Duretz et al., 2016). Erosion and sedimentation is mimicked by a linear diffusion of the topography. Where deposition occurs, the material parameters of sediments (Table S1) are assigned to the newly appearing material. Densities are calculated with an equation of state using compressibility and thermal expansion factors. Applied parameters are given in Table S1.

The applied numerical algorithm solves the partial differential equations of continuum mechanics for 2D slow deformations (no inertia) coupled with heat transfer under gravity. The force balance equations are:

$$\frac{\partial \sigma_{ij}}{\partial x_j} = -\rho b_i, \quad (1)$$

where  $i$  and  $j$  are indexes of either 1 or 2 and represent the horizontal x-direction ( $i, j = 1$ ) and vertical y-direction ( $i, j = 2$ ),  $b_1 = 0$  and  $b_2 = g$ .  $\sigma_{ij}$  are the total Maxwell-visco-elastic stress tensor components, which are expressed using a backward-Euler rule (e.g. Schmalholz et al., 2001) by

$$\sigma_{ij} = -P + 2 \left( \frac{1}{\eta_{\text{diss}}} + \frac{1}{G\Delta t} \right)^{-1} \dot{\epsilon}_{ij} + \left( 1 + \frac{G\Delta t}{\eta_{\text{diss}}} \right)^{-1} \sigma_{ij}^o + J_{ij}, \quad (2)$$

where  $P$  corresponds to the pressure,  $\dot{\epsilon}_{ij}$  are the components of the deviatoric strain rate tensor,  $G$  is the shear modulus,  $\eta$  is the effective viscosity,  $\Delta t$  is the numerical time step,  $\sigma_{ij}^o$  are the stress tensor components from the previous time step and  $J_{ij}$  includes all the corresponding terms resulting from the Jaumann rate of the stress tensor (e.g. Beuchert & Podladchikov, 2010).

The rheological model is based on the additive decomposition of the deviatoric strain rate tensor  $\dot{\epsilon}_{ij}$ :

$$\dot{\epsilon}_{ij} = \dot{\epsilon}_{ij}^{\text{el}} + \dot{\epsilon}_{ij}^{\text{pl}} + \dot{\epsilon}_{ij}^{\text{dis}} + \dot{\epsilon}_{ij}^{\text{dif}} + \dot{\epsilon}_{ij}^{\text{Pei}}. \quad (3)$$

where  $\dot{\epsilon}_{ij}^{\text{el}}$ ,  $\dot{\epsilon}_{ij}^{\text{pl}}$ ,  $\dot{\epsilon}_{ij}^{\text{dis}}$ ,  $\dot{\epsilon}_{ij}^{\text{dif}}$  and  $\dot{\epsilon}_{ij}^{\text{Pei}}$  correspond to the strain rate contributions arising from elasticity, plasticity and viscous creep (dislocation, diffusion and Peierls), respectively. This strain rate equation is nonlinear and solved locally on cell centroids and vertices in order to define the current effective viscosity and stress (e.g. Popov & Sobolev, 2008). The viscosity, for any kind of creep, is formulated as a function of the corresponding strain rate invariant.

The viscosity for diffusion and dislocation creep is

$$\eta^X = (FAd^m)^{-\frac{1}{n}} \left( \dot{\epsilon}_{\text{II}}^X \right)^{\frac{1}{n}-1} \exp \left( \frac{Q}{nRT} \right) \quad (4)$$

where either  $X = \text{dif}$  or  $X = \text{dis}$ .

$$F = 2^{n-1} 3^{\frac{n+1}{2}} \quad (5)$$

is a factor, needed to convert flow law parameters from axial compression experiments into an invariant form (e.g. Gerya, 2009). The other parameters are displayed and explained in Table S1.

Peierls creep (i.e. low-temperature plasticity) is applied in both the lithospheric and asthenospheric mantle, using the approach from

Kameyama et al. (1999):

$$\eta^{\text{Pei}} = F_{\text{Pei}} A \left( \dot{\epsilon}_{\text{II}}^{\text{Pei}} \right)^{\frac{1}{S(T)} - 1} \exp \left( \frac{Q}{RT} \frac{(1 - \gamma)^q}{S(T)} \right) \gamma \sigma_{\text{P}}, \quad (6)$$

where an effective stress exponent that depends on the temperature is

$$S(T) = 2\gamma \frac{Q}{RT} (1 - \gamma), \quad (7)$$

and

$$F_{\text{Pei}} = 2^{-\frac{1-S(T)}{S(T)}} 3^{-\frac{1+S(T)}{2S(T)}} \quad (8)$$

is the geometry factor, specific for the presented Peierls formulation. For the rest of the parameters see Table S1.

The stress of all material phases is limited by a yield stress,  $\tau_y$ , defined by the Drucker–Prager criterion:

$$\tau_y = C \cos(\phi) + P \sin(\phi). \quad (9)$$

In case of yielding, the effective viscosity is computed such that the stress invariant equals the yield stress (e.g. Lemiale et al., 2008; Schmalholz & Maeder, 2012). Therefore, the effective viscosity for plasticity is computed only for  $\tau_{\text{II}} \geq \tau_y$  and takes the form of:

$$\eta^{\text{pl}} = \frac{\tau_y}{2\dot{\epsilon}_{\text{II}}^{\text{eff}}} \quad \text{where,} \quad \dot{\epsilon}_{ij}^{\text{eff}} = \dot{\epsilon}_{ij} + \frac{\tau_{ij}}{2G\Delta t} \quad (10)$$

At the end of the local iteration cycle, the effective viscosity is equal to the quasi-harmonic mean of the viscosities of each dissipative deformation mechanism:

$$\eta_{\text{diss}} = \left( \frac{1}{\eta^{\text{dis}}} + \frac{1}{\eta^{\text{dif}}} + \frac{1}{\eta^{\text{Pei}}} + \frac{1}{\eta^{\text{pl}}} \right)^{-1} \quad (11)$$

The applied 2-D equation for heat transfer is:

$$\rho C_p \frac{dT}{dt} = \frac{\partial}{\partial x_i} \left( k \frac{\partial T}{\partial x_i} \right) + Q_{\text{SH}} + Q_{\text{R}}, \quad (12)$$

where  $Q_{\text{R}}$  is the radiogenic heat production and  $Q_{\text{SH}} = (\tau_{11}^2 + \tau_{22}^2 + 2\tau_{12}^2)/2\eta$  is the heat production due to viscous and plastic dissipative work. In this study we assume that all dissipative work is converted into heat (i.e. the so-called Taylor–Quinney coefficient is 1).

## References

- Beuchert, M. J. & Podladchikov, Y. Y., 2010. Viscoelastic mantle convection and lithospheric stresses, *geophysical Journal international*, **183**(1), 35–63.
- Carter, N. L. & Tsenn, M. C., 1987. Flow properties of continental lithosphere, *Tectonophysics*, **136**(1-2), 27–63.
- Duretz, T., May, D. A., & Yamato, P., 2016. A free surface capturing discretization for the staggered grid finite difference scheme, *Geophysical Journal International*, **204**(3), 1518–1530.
- Gerya, T., 2009. *Introduction to numerical geodynamic modelling*, Cambridge University Press.
- Gerya, T. V. & Yuen, D. A., 2003. Characteristics-based marker-in-cell method with conservative finite-differences schemes for modeling geological flows with strongly variable transport properties, *Physics of the Earth and Planetary Interiors*, **140**(4), 293–318.
- Hirth, G. & Kohlstedt, D., 2003. Rheology of the upper mantle and the mantle wedge: A view from the experimentalists, *Inside the subduction Factory*, pp. 83–105.
- Kameyama, M., Yuen, D. A., & Karato, S.-I., 1999. Thermal-mechanical effects of low-temperature plasticity (the peierls mechanism) on the deformation of a viscoelastic shear zone, *Earth and Planetary Science Letters*, **168**(1-2), 159–172.
- Lemiale, V., Mühlhaus, H.-B., Moresi, L., & Stafford, J., 2008. Shear banding analysis of plastic models formulated for incompressible viscous flows, *Physics of the Earth and Planetary Interiors*, **171**(1-4), 177–186.
- Mackwell, S., Zimmerman, M., & Kohlstedt, D., 1998. High-temperature deformation of dry diabase with application to tectonics on venus, *Journal of Geophysical Research: Solid Earth*, **103**(B1), 975–984.
- Popov, A. & Sobolev, S., 2008. Slim3d: A tool for three-dimensional thermomechanical modeling of lithospheric deformation with elasto-visco-plastic rheology, *Physics of the Earth and Planetary Interiors*, **171**(1-4), 55–75.
- Ranalli, G., 1995. *Rheology of the Earth*, Springer Science & Business Media.
- Schmalholz, S., Podladchikov, Y., & Schmid, D., 2001. A spectral/finite difference method for simulating large deformations of heterogeneous, viscoelastic materials, *Geophysical Journal International*, **145**(1), 199–208.
- Schmalholz, S. M. & Maeder, X., 2012. Pinch-and-swell structure and shear zones in viscoplastic layers, *Journal of Structural Geology*, **37**, 75–88.
- Schmalholz, S. M., Duretz, T., Hetényi, G., & Medvedev, S., 2019. Distribution and magnitude of stress due to lateral variation of gravitational potential energy between indian lowland and tibetan plateau, *Geophysical Journal International*, **216**(2), 1313–1333.

**Table S1.** Table and list of model parameters, where  $A$  is the pre-exponential factor,  $n$  is the power-law exponent,  $Q$  is the activation energy,  $V$  is the activation volume,  $\lambda$  is the thermal conductivity,  $d$  is the grain size,  $m$  is the grain-size exponent,  $\sigma_P$  is Peierls stress,  $q$  is the Peierls exponent,  $\rho_{ref}$  is the density at reference pressure ( $P_{ref} = 0$  Pa) and temperature ( $T_{ref} = 0$  °C),  $Q_R$  is the radioactive heat production. Some parameters have constant values:  $C_p = 1050$  J.K<sup>-1</sup> is the heat capacity,  $G = 2 \times 10^{10}$  Pa is the shear modulus,  $\alpha = 3 \times 10^5$  K<sup>-1</sup> is the thermal expansion coefficient,  $\beta = 10^{-11}$  Pa<sup>-1</sup> is the compressibility,  $C = 10^7$  [Pa] is the cohesion,  $\phi = 30^\circ$  is the friction angle, and  $\gamma = 0.1$  is an adjustable constant. The effective pre-exponent ( $A_{eff} = FAd^m$ ) is used for the temperature prediction (' $A$ ' in equation 1 of the main text). For the crust, the conductivities ( $\lambda$ ), used for model (1) are displayed and the conductivities used for models (2) and (3) are in the parentheses. For the mantle, the lithospheric conductivities are displayed and the asthenospheric conductivities are in the parentheses. Sources of rheological parameters: <sup>1</sup> wet quartzite (Ranalli, 1995), <sup>2</sup> westerly granite (Carter & Tsenn, 1987), <sup>3</sup> Maryland diabase (Mackwell et al., 1998), <sup>4</sup> dry olivine (Hirth & Kohlstedt, 2003), <sup>5</sup> dry olivine (Kameyama et al., 1999). The erosional diffusivity for modelling the surface evolution with a linear diffusion equation is  $D = 3 \times 10^{-5}$  m<sup>2</sup>.s<sup>-1</sup>.

Lithology	$A$ [Pa <sup>-n</sup> m <sup>-m</sup> s <sup>-1</sup> ]	$n$	$Q$ [J.mol <sup>-1</sup> ]	$V$ [m <sup>3</sup> .mol <sup>-1</sup> ]	$\lambda$ [W.m <sup>-1</sup> K <sup>-1</sup> ]	$d$ [m]	$m$	$\sigma_P$ [Pa]	$q$	$\rho_{ref}$ [kg.m <sup>-3</sup> ]	$Q_R$ [W.m <sup>-3</sup> ]
Sediments <sup>1</sup>	$5.07 \times 10^{-18}$	2.3	$1.54 \times 10^5$	0	2.40	-	0	-	0	2800	$0.8 \times 10^{-6}$
Upper crust <sup>2</sup>	$3.16 \times 10^{-26}$	3.3	$1.87 \times 10^5$	0	2.40 (2.25)	-	0	-	0	2800	$1.47 \times 10^{-6}$
Lower crust <sup>3</sup>	$5.05 \times 10^{-28}$	4.7	$4.85 \times 10^5$	0	2.40 (2.25)	-	0	-	0	2900	$1.47 \times 10^{-6}$
Mantle <sub>dis</sub> <sup>4</sup>	$1.10 \times 10^{-16}$	3.5	$5.30 \times 10^5$	$1.4 \times 10^{-5}$	2.25 (41.25)	-	0	-	0	3350	$2.11 \times 10^{-10}$
Mantle <sub>dif</sub> <sup>4</sup>	$1.50 \times 10^{21}$	1.0	$3.75 \times 10^5$	$8.0 \times 10^{-6}$	2.25 (41.25)	$10^{-3}$	-3	-	0	3350	$2.11 \times 10^{-10}$
Mantle <sub>Pei</sub> <sup>5</sup>	$5.7 \times 10^{11}$	-	$5.36 \times 10^5$	0	2.25 (41.25)	-	0	$8.5 \times 10^9$	2	3350	$2.11 \times 10^{-10}$

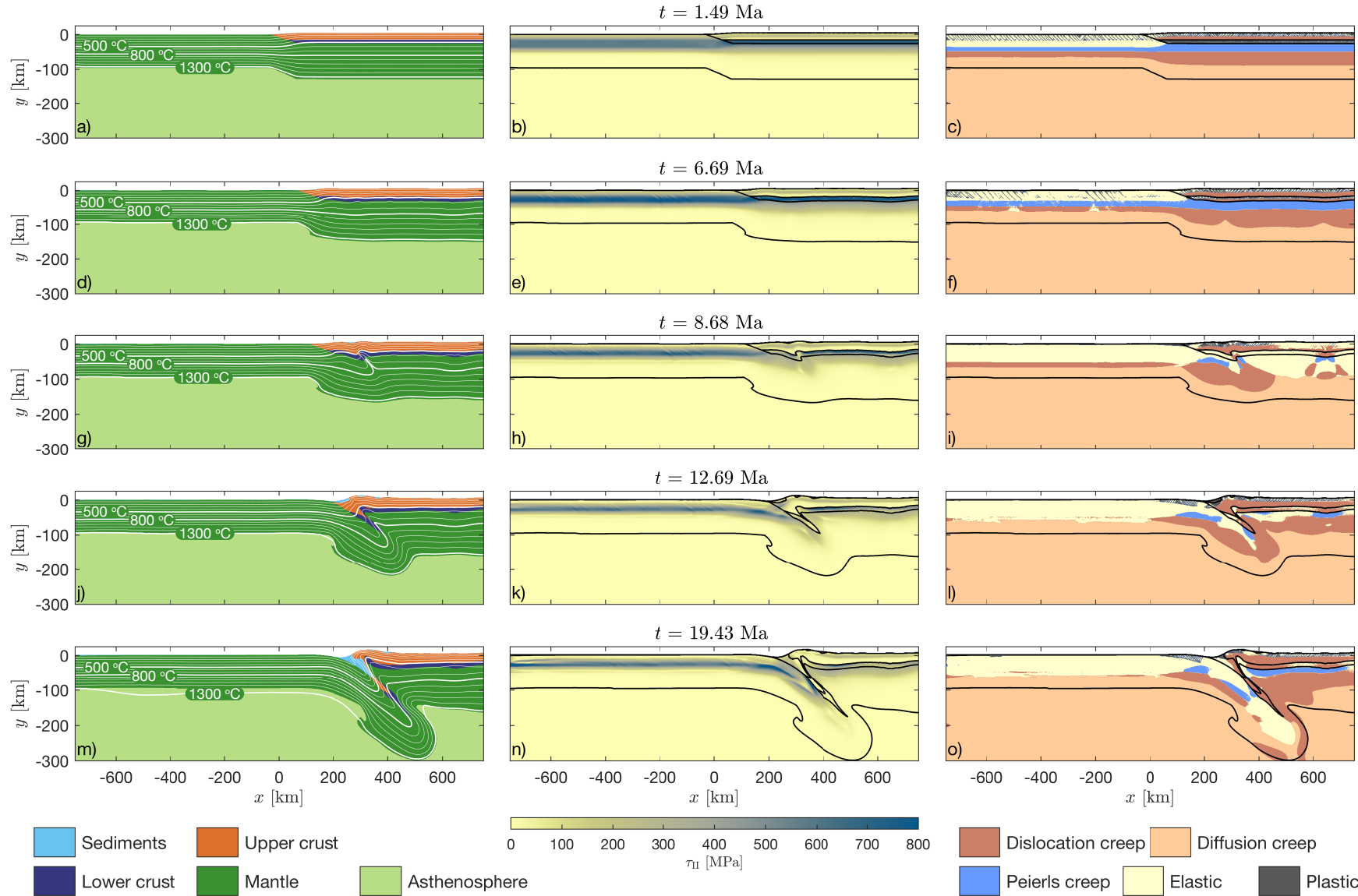


**Figure S1.** Evolution of model geometry (left column), stress field (middle column) and distribution of dominant deformation mechanism (right column) for simulation (1). Left column: White lines indicate isotherms every 100 °C and coloured field indicate different model units; see legend below left column. Middle column: Stress is quantified with the second invariant of deviatoric stress tensor. Black lines indicate from bottom to top: lithosphere-asthenosphere boundary, Moho and upper-lower crust boundary. Right column: The dominant deformation mechanism is the one corresponding to the largest strain rate contribution (see equation 3).

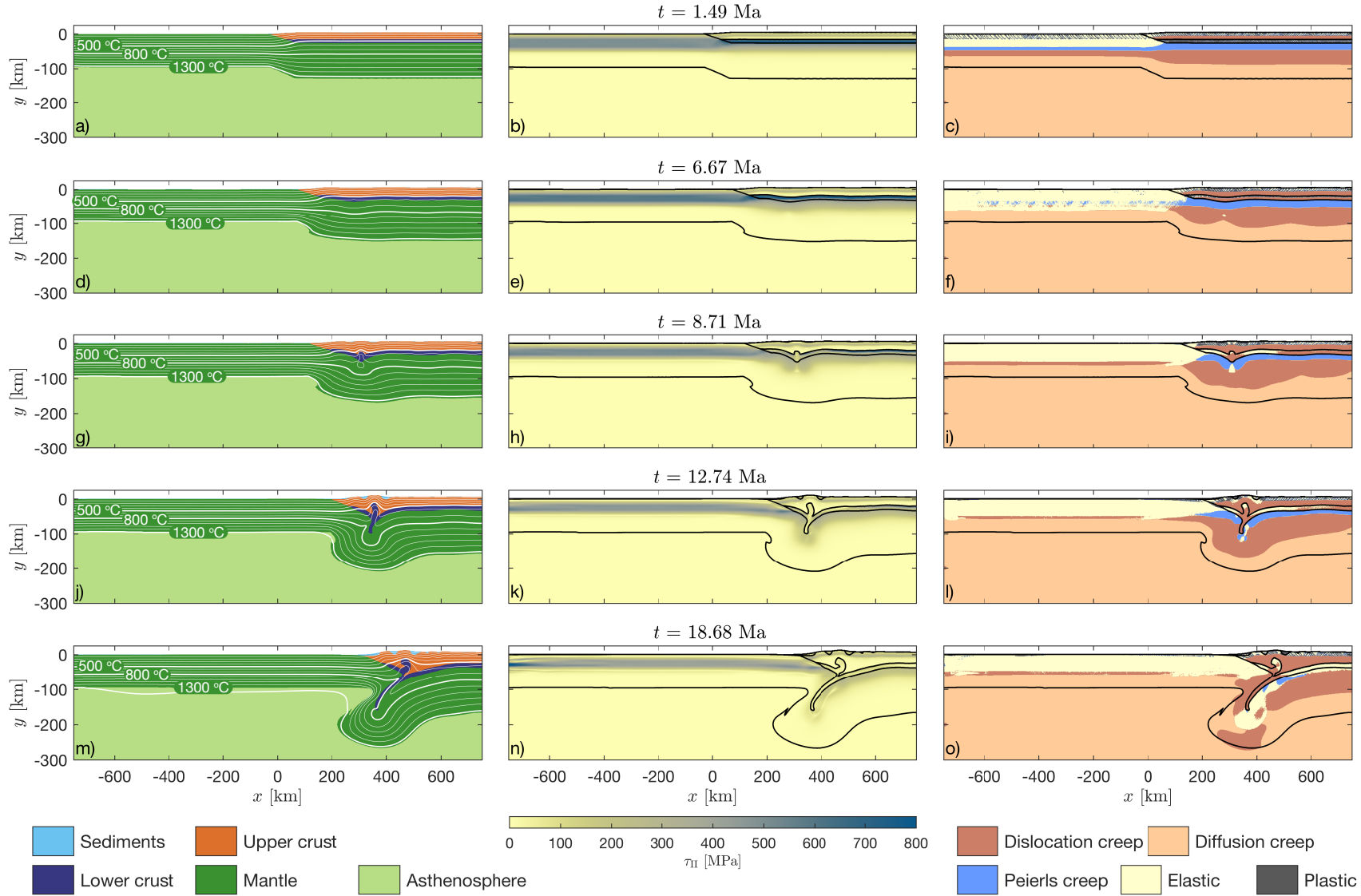


**Figure S2.** Evolution of model geometry (left column), stress field (middle column) and distribution of dominant deformation mechanism (right column) for simulation (2). Left column: White lines indicate isotherms every 100 °C and coloured field indicate different model units; see legend below left column. Middle column: Stress is quantified with the second invariant of deviatoric stress tensor. Black lines indicate from bottom to top: lithosphere-asthenosphere boundary, Moho and upper-lower crust boundary. Right column: The dominant deformation mechanism is the one corresponding to the largest strain rate contribution (see equation 3).

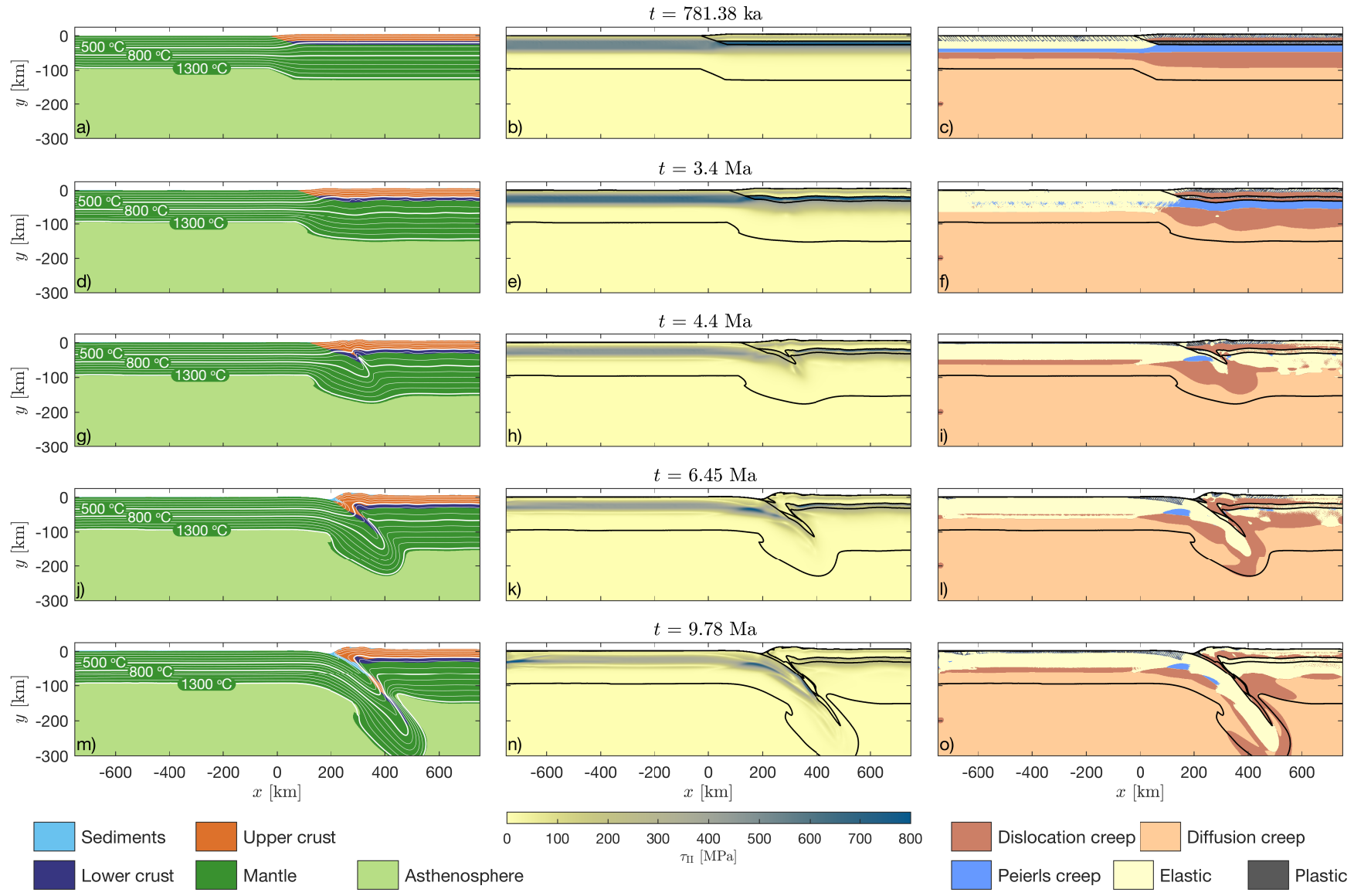


**Figure S3.** Evolution of model geometry (left column), stress field (middle column) and distribution of dominant deformation mechanism (right column) for simulation (3). Left column: White lines indicate isotherms every 100 °C and coloured field indicate different model units; see legend below left column. Middle column: Stress is quantified with the second invariant of deviatoric stress tensor. Black lines indicate from bottom to top: lithosphere-asthenosphere boundary, Moho and upper-lower crust boundary. Right column: The dominant deformation mechanism is the one corresponding to the largest strain rate contribution (see equation 3).

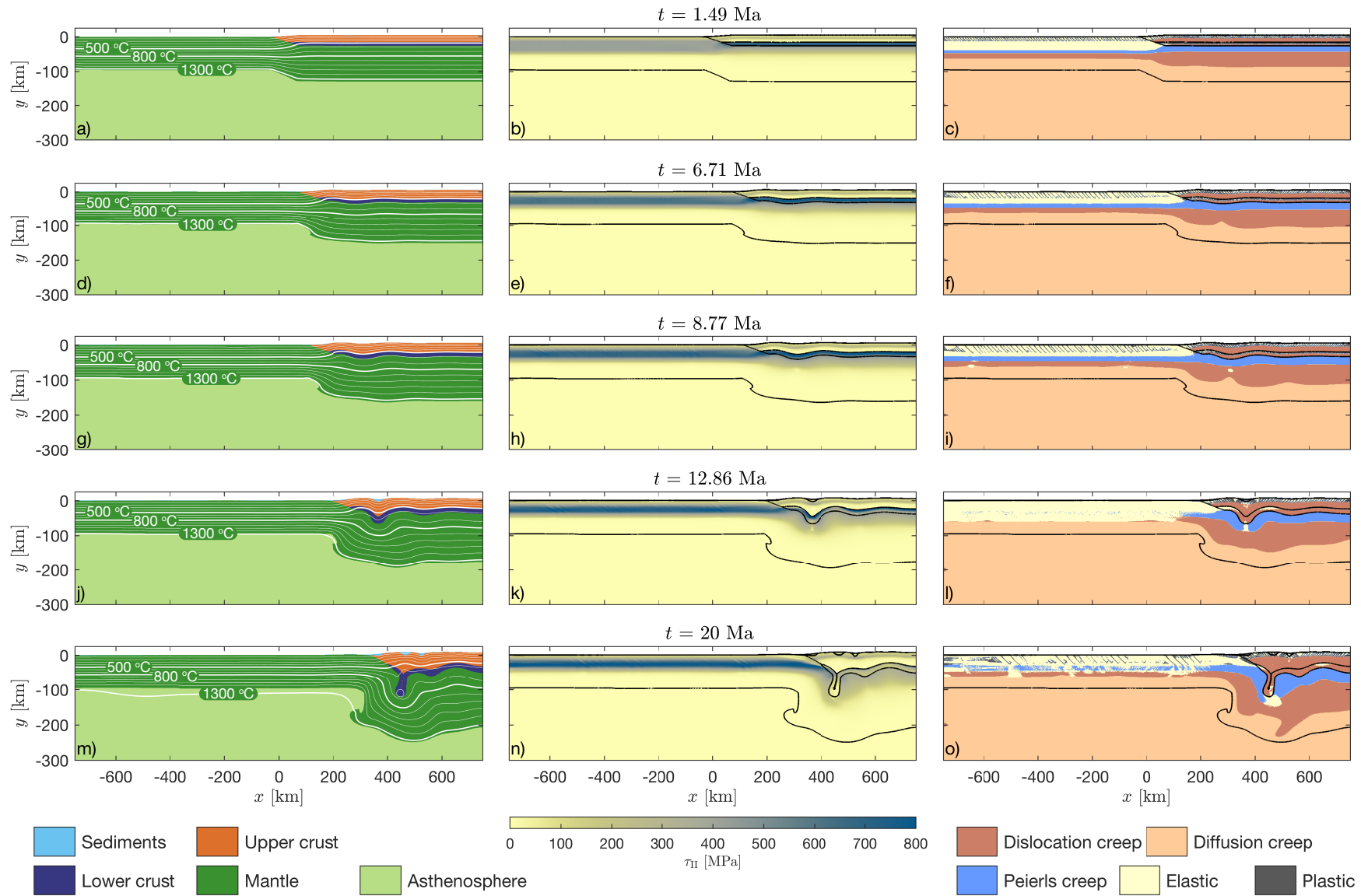


**Figure S4.** Evolution of model geometry (left column), stress field (middle column) and distribution of dominant deformation mechanism (right column) for simulation (4). Left column: White lines indicate isotherms every 100 °C and coloured field indicate different model units; see legend below left column. Middle column: Stress is quantified with the second invariant of deviatoric stress tensor. Black lines indicate from bottom to top: lithosphere-asthenosphere boundary, Moho and upper-lower crust boundary. Right column: The dominant deformation mechanism is the one corresponding to the largest strain rate contribution (see equation 3).

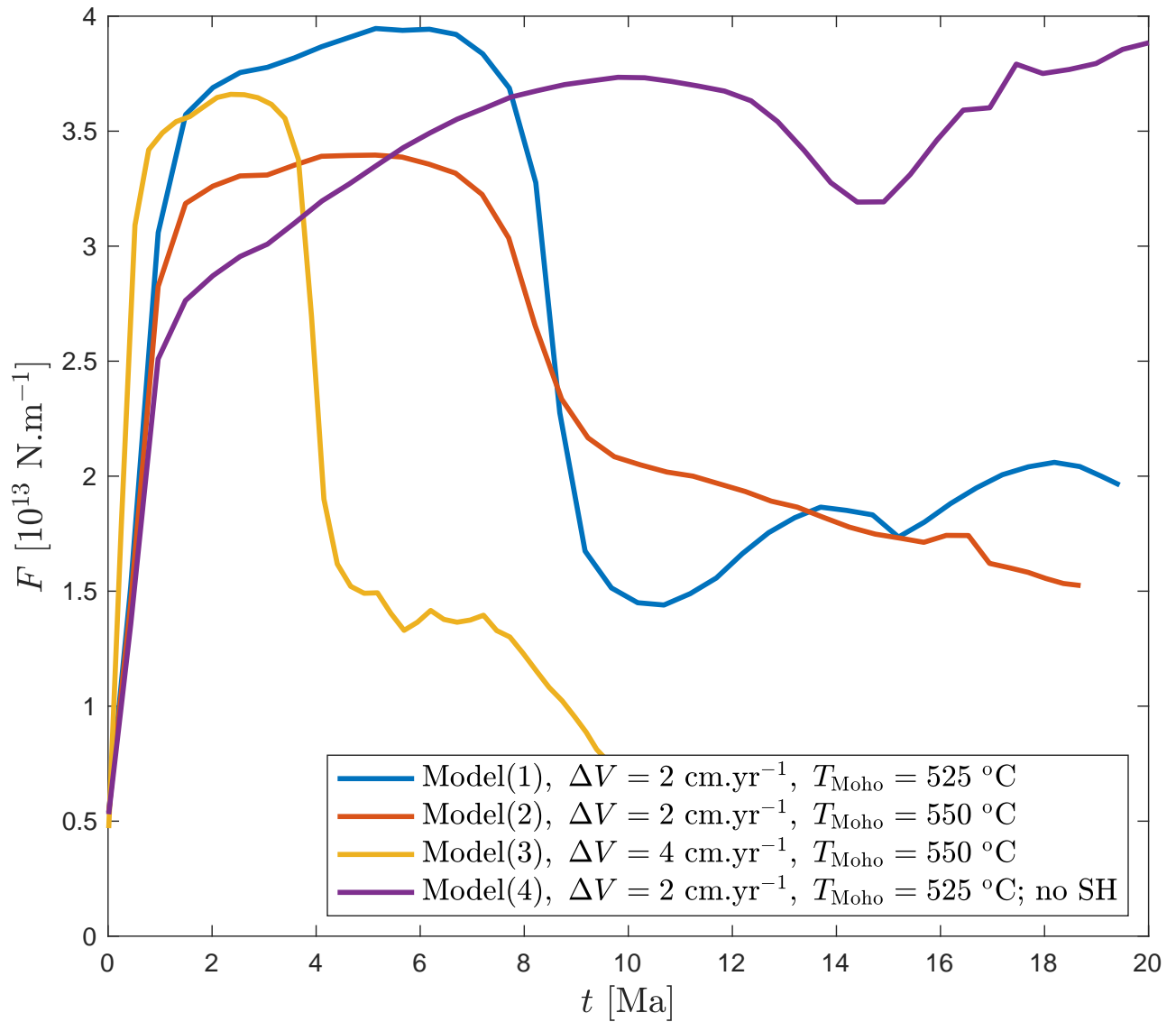


**Figure S5.** Evolution of the horizontal driving force (per unit length) with time for all four simulations. The driving force is the vertically integrated difference between the horizontal total stress,  $\sigma_{xx}$  and lithostatic pressure). The driving forces were calculated at x-position = -250 km.

**Movie S1:** Colourplot of temperature change, with respect to initial temperature, of material points,  $\Delta T$ , for model (1) at specific simulation times,  $t$ . For better visibility the colour bar is saturated at 250 °C. Values of  $T_{SH}$  are calculated with equation (1, main text) for parameters of mantle dislocation creep (Table S1), corresponding convergence velocity and simulation time. Isotherms are plotted for corresponding  $T_{SH}$  and  $T_{SH} \pm 100$  °C (see legend). The yellow contours bound the area with significant dissipation,  $Q_{SH} \geq 10 \mu W.m^{-3}$ .

This movie is a representative example of the transient nature of shear heating during subduction initiation. A few million years after strain localisation in the mantle lithosphere (ca 40 km slip along the shear zone), shear heating is diminishing due to the weak upper-crustal material, that is lubricating the subduction interface (our model does not include the strengthening of rocks during prograde metamorphism).

**2 FOR EDITORS**

This paper has been produced using the Blackwell Scientific Publications GJI L<sup>A</sup>T<sub>E</sub>X2e class file.